Cell Reports
Physical Science

CellPress
OPEN ACCESS

Article

A lanthanide-doped glass-ceramic fiber for stress sensing

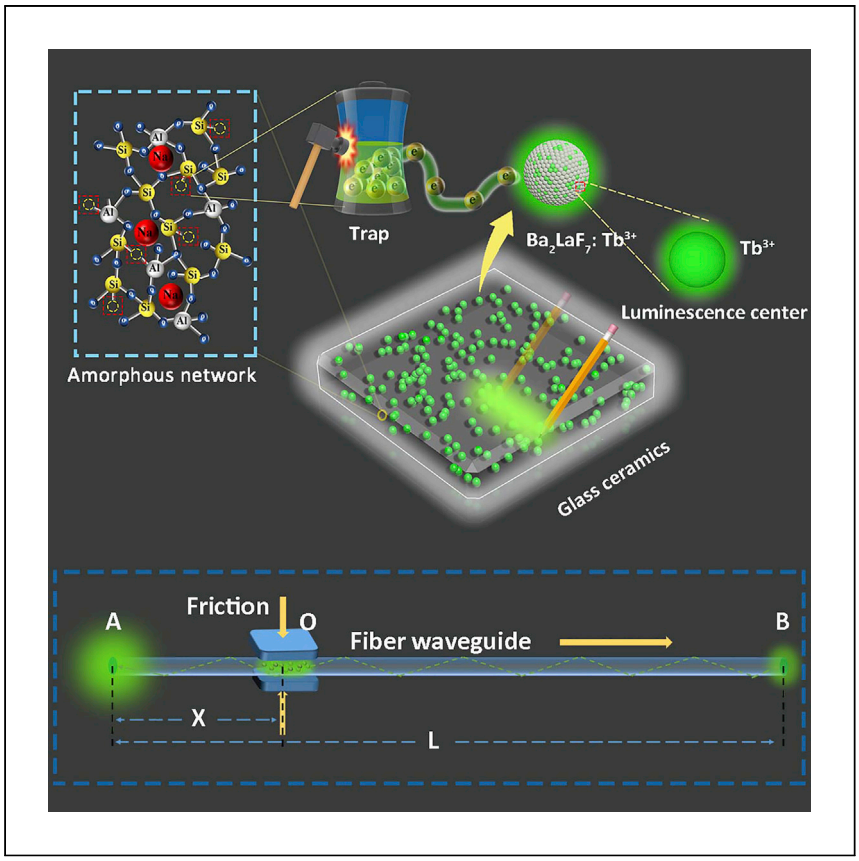

Tang et al. demonstrate bright green mechanoluminescence from a transparent glass ceramic. The transparent medium developed in this work not only accurately records stress signals but also provides a promising strategy for transmission of the recorded signals.

Haitao Tang, Lei Zhao, Zhichao Liu, ..., Ting Wang, Jianbei Qiu, Xuhui Xu

yuyu6593@126.com (X.Y.)
zhfwang@licp.cas.cn (Z.W.)
xuxuh07@126.com (X.X.)

Highlights

Bright green mechanoluminescence is observed from terbium-doped fluoride nanocrystals in a transparent medium

An optical fiber is developed and implemented as a remote stress sensor

The explored transparent mechanoluminescent stress sensor is self-driven, free from external power

Tang et al., Cell Reports Physical Science 3, 101093
October 19, 2022
https://doi.org/10.1016/j.xcrp.2022.101093

Cell Reports
Physical Science

CellPress
OPEN ACCESS

Article

A lanthanide-doped glass-ceramic fiber for stress sensing

Haitao Tang,[1,6] Lei Zhao,[2,6] Zhichao Liu,[1] Qingpeng Peng,[1] Xue Yu,[3,*] Qingyuan Wang,[3] Feng Zhao,[3] Mao Deng,[3] Yongqing Bai,[4] Zhaofeng Wang,[4,*] Ting Wang,[5] Jianbei Qiu,[1] and Xuhui Xu[1,7,*]

SUMMARY

Stress sensors that can recognize the location where a force is applied and propagate strain information are desirable for future integrated intelligent devices. However, developing sensors free from electromagnetic interference and complicated detector setups is challenging. Here, a self-driven optical fiber is developed and implemented as a remote stress sensor. Terbium-doped fluoride nanocrystals (Ba_2LaF_7: Tb^{3+}) are precipitated *in situ* from a transparent glass and have notable mechanoluminescence (ML) because of designed defect traps. We propose that the encapsulated nature of the nanocrystals (NCs) within the amorphous matrix facilitates efficient energy transfer from traps to emission centers, which is critical for achieving the ML behavior. The optical waveguide effect of the as-developed transparent ML sensor facilitates capture and transmission of the signals. The explored self-driven glass ceramic fiber opens a door for detecting and recording mechanical information within integrated devices.

INTRODUCTION

Development of intelligent terminals for artificial intelligence, smart homes, and transportation has received sustained attention,[1–4] where sensors are essential _components that play an important role in the evolution of the corresponding devices. Currently, stress sensors are urgently needed for practical applications in human-computer interactions, intelligent skins, biohealth monitoring, and so on.[2,5,6] Nevertheless, traditional electronic stress sensors (including piezoelectric, capacitive, and resistive detectors) are dependent on the piezoelectric and piezoresistive effects, which do not work safely and reliably in harsh environments because of their poor immunity to electromagnetic interference.[1–3] Complex equipment, including an additional power supply and electrical signal processing systems, is necessary for the capture and detection of force signals (Figure S1). Compared with their electronic counterparts, optical fiber-based stress sensors—sensors that transform mechanical stress into optical parameters, such as light intensity[7] or optical phase deviation wavelengths[8]—have advantages, including immunity against electromagnetic interference as well as increased feasibility of distributed and remote sensing.[9] Fiber grating stress sensors based on optical signal transmission have been developed and have fascinating long-distance and rapid responses.[8,9] Unfortunately, the requirements for micron and nanometer gratings, high-precision demodulators, and additional light sources increase the technical costs of the fiber grating and severely limit their practical application.

Mechanoluminescent materials convert mechanical energy into light in response to external mechanical stimulation, such as friction, tension, fracture, impact, and

[1]Faculty of Materials Science and Engineering, Key Laboratory of Advanced Materials of Yunnan Province, Kunming University of Science and Technology, Kunming, Yunnan 650093, P.R. China

[2]School of Physics and Opto-Electronic Technology, Baoji University of Arts and Sciences, Baoji, Shaanxi 721016, P.R. China

[3]School of Mechanical Engineering, Institute for Advanced Study, Institute for Advanced Materials Deformation and Damage from Multi-Scale, Chengdu University, Chengdu 610106, P.R. China

[4]State Key Laboratory of Solid Lubrication, Lanzhou Institute of Chemical Physics, Chinese Academy of Sciences, Lanzhou 730000, P.R. China

[5]College of Materials and Chemistry & Chemical Engineering, Chengdu University of Technology, Chengdu 610059, P.R. China

[6]These authors contributed equally

[7]Lead contact

*Correspondence: yuyu6593@126.com (X.Y.), zhfwang@licp.cas.cn (Z.W.), xuxuh07@126.com (X.X.)

https://doi.org/10.1016/j.xcrp.2022.101093

compression.[10] Accordingly, mechanoluminescent stress sensors are particularly attractive for self-driven stress-sensing technology based on monitoring optical signals for wireless remote detection and nondestructive analysis. Immunity to electromagnetic interference ensures reliability of the signals.[11] The self-powering ability of stress-to-photon transduction units without electronic conduction simplifies system construction for force detection.[12–16] Enormous effort has been devoted to finding superior mechanoluminescence (ML) performance. Explored mechanoluminescent materials are typically encased and embedded within organic polymers (polydimethylsiloxane, polymethylmethacrylate, silica gel, etc.)[17–19] to achieve force distribution with attachment to the target. Although the available soft organic polymer matrices enable visualization of the dynamic stress distribution generated from fracto-[13], tribo-,[20,21] and elastico-ML,[15] it is acknowledged that the non-uniform distribution of the corresponding encapsulated mechanoluminescent materials with micron size and the opacity of the matrices fail to accurately realize presentation and transmission of stress signals in a timely manner, with inevitable optical loss.[18,19]

Glass, a traditional transparent medium with amorphous structure, promises propagation of light.[22–24] Producing ML in the transparent medium of glass is a promising alternative to simultaneously realize generation and transmission of force signals. However, a general approach is lacking to achieve ML performance within an amorphous matrix because of the failure to effectively manipulate defects,[25] which are considered to be prerequisites for obtaining elastico-ML.

Here, uniform terbium-doped fluoride Ba_2LaF_7 nanocrystals (NCs) are produced *in situ* by a controlled crystallization procedure and, within an amorphous transparent medium, perform bright ML because of deliberately introduced defect states. The remote real-time response of stress signals and the accurate location of the force are recognized, taking advantage of the optical waveguide characteristics of the transparent medium. Hence, the innovative strain sensor in the transparent ML medium records long-distance transmission of stress signals in an accurate and timely fashion. This work opens a new door for self-driven integrated stress-sensing devices.

RESULTS AND DISCUSSION

Crystal structure and micromorphology of the Ba_2LaF_7: 4.0Tb^{3+} glass ceramic

Figures 1A and S2A show the X-ray diffraction (XRD) patterns of the as-prepared Ba_2LaF_7: xTb^{3+} (x = 3.0, 3.5, 4.0, 4.5, and 5.0) glass ceramic (GC) samples, which well matches the standard profile (JCPDS 48-0099) of Ba_2LaF_7. It indicates that the pure phase is obtained for the insignificant effect of incorporation of Tb^{3+} ions on the crystal structure. The elemental mapping images (Figure S2B) illustrate the uniform distribution of the corresponding elements of the precipitated particles. The transmission electron microscopy (TEM), the high-angle annular dark-field scanning TEM (HAADF-STEM), and the corresponding fast Fourier transform (FFT) image of the sample are given in Figures 1B and 1C, respectively. They reveal the aligned atoms of the precipitated Ba_2LaF_7: Tb^{3+} NCs encased within the amorphous glass matrix. We performed *in situ* TEM imaging at a heating temperature of 430°C (Figure 1D; Video S1), which clearly illustrates the phase separation, nucleation, and gradual growth of these Ba_2LaF_7 nanoparticles. The *in situ* high-resolution TEM (HR-TEM) images (Figure 1E; Video S2) demonstrate that the nanoclusters are free from crystallization as recorded at 0 s, and the corresponding inverse FFT (IFFT) images clearly show that the (200) and (220) crystal planes of Ba_2LaF_7 appear at 12 s, and, subsequently, the (400) crystal plane emerges at

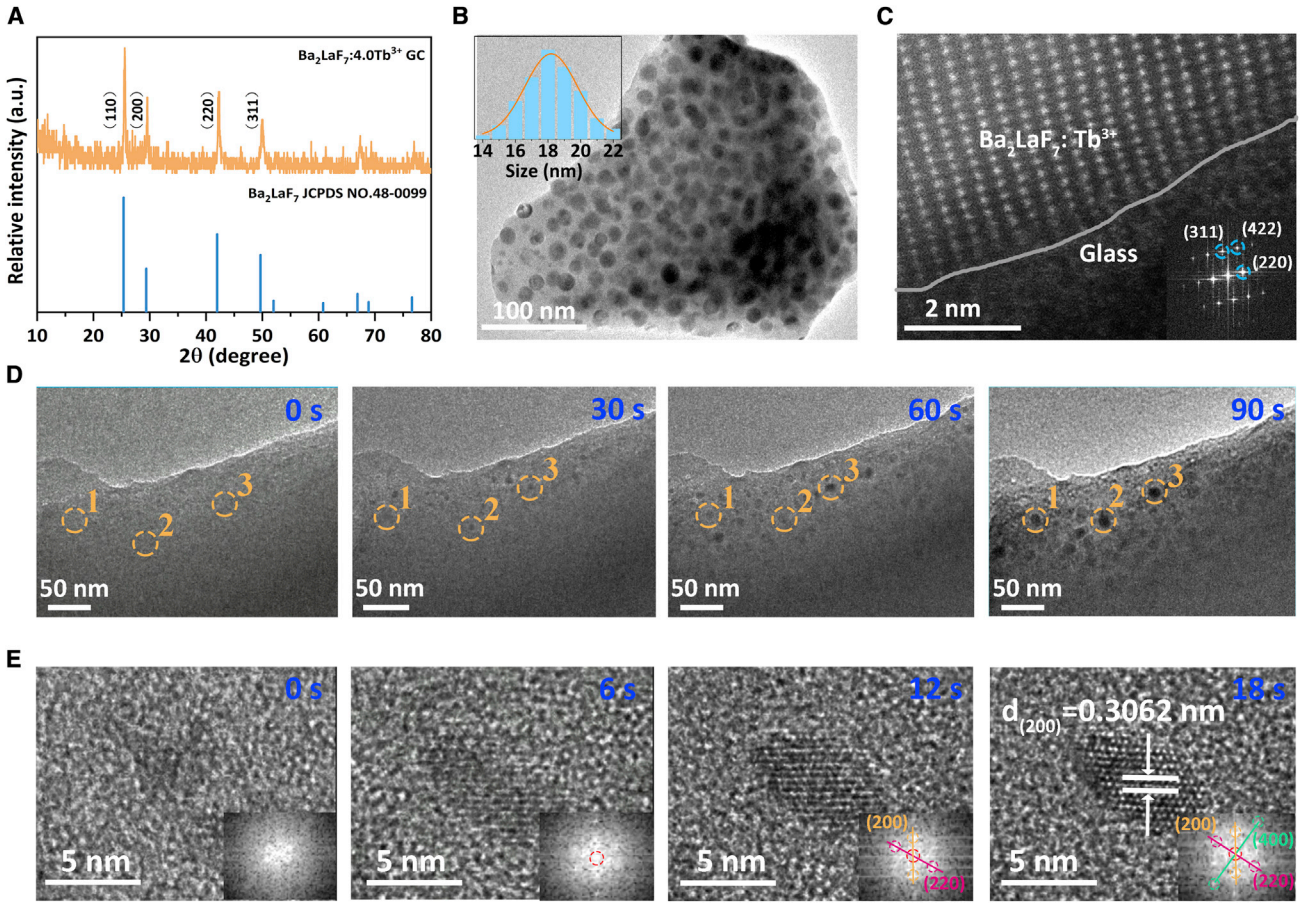

Figure 1. Microstructure characterization of the Ba_2LaF_7: 4.0Tb^{3+} glass ceramic (GC)

(A) XRD patterns.

(B) TEM image (inset: particle size distribution histogram; scale bar, 100 nm).

(C) HAADF-STEM image (inset: the corresponding FFT image; scale bar, 2 nm).

(D and E) *In situ* TEM (D; scale bar, 50 nm) and the corresponding HRTEM images (E; inset: the corresponding IFFT images; scale bar: 5 nm) recorded at 430°C for 0∼90 s of the Ba_2LaF_7: 4.0Tb^{3+} GC. The electron beam intensity was set to be 2.7 A/cm^2.

18 s. NCs grown via a controlled crystallization procedure with a small size and uniform distribution are critical to ensure the transparency of GCs and achieve an effective optical waveguide effect.[26] In this work, small Ba_2LaF_7 NC are obtained by inhibition of the three-dimensional network structure provided by the inorganic transparent medium. The high viscosity of the transparent medium ensures that Ba_2LaF_7 crystals with a particle size of 18.20 nm are precipitated (Figure 1B).

ML performance of the Ba_2LaF_7: 4.0Tb^{3+} GC

The transmittance of the Ba_2LaF_7: 4.0 Tb^{3+} GC reaches 80% in the visible region ranging from 400–800 nm (Figure S3A). A femtosecond laser (800 nm) is employed as an excitation light source in this work to fulfill the constructed traps (Figure S4). The ML spectra and thermoluminescence (TL) glow curves of these GC samples with different doping concentrations of Tb^{3+} are presented in Figure S5, where Ba_2LaF_7: 4.0Tb^{3+} performs an optimized performance with maximum ML intensity. The ML performance from the transparent matrix recorded in the dark (Video S3) and under daylight irradiation (Video S4) is presented in Figure 2A. The ML can be

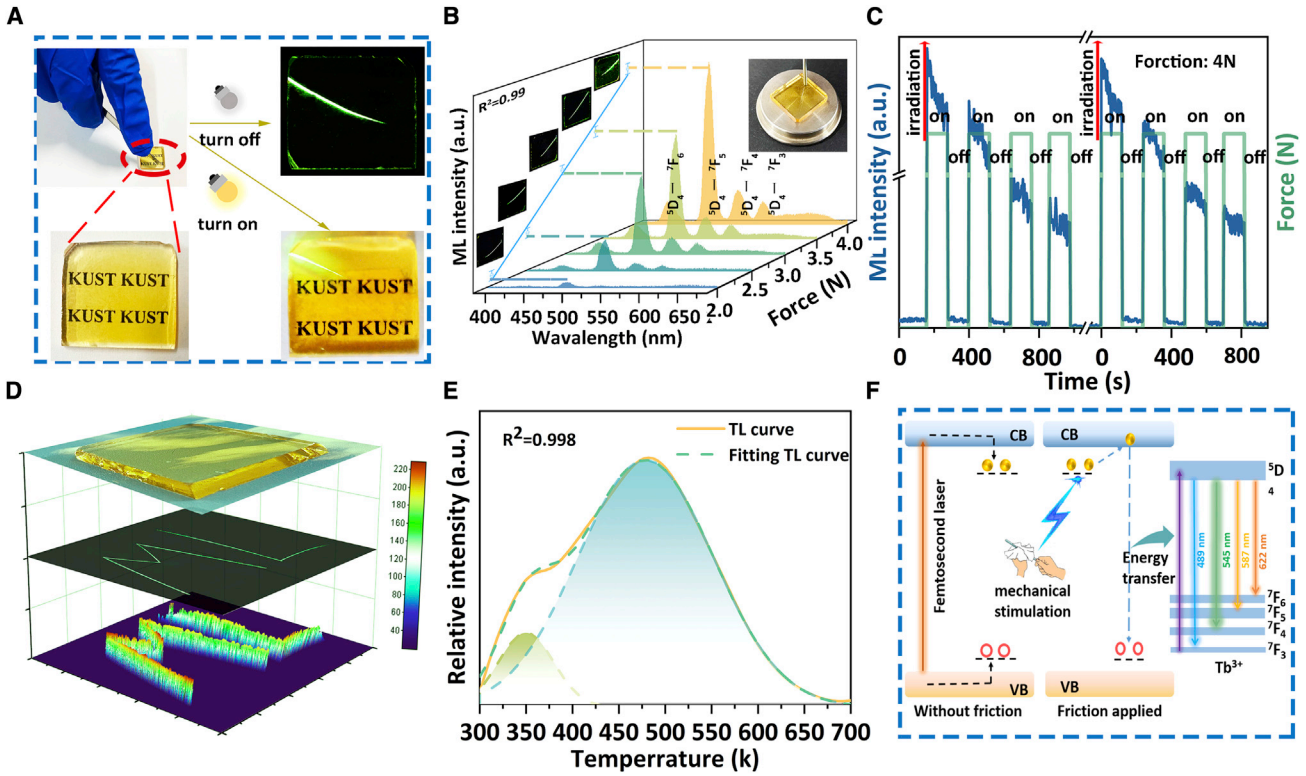

Figure 2. ML performance of the Ba_2LaF_7: 4.0 Tb^{3+} GC

(A) Photographs recorded in the dark and daylight under friction stimulation.

(B) ML spectra dependent on the loaded force (left inset: the corresponding ML image; right inset: the test platform).

(C) The plotted ML intensity of the Ba_2LaF_7: 4.0 Tb^{3+} GC recorded with a periodically loaded force of 4 N.

(D) Visualization of a handwriting trajectory through longtime exposure and the distribution of relative ML intensity extracted from the corresponding ML image according to the grayscale value.

(E) TL spectrum of the Ba_2LaF_7: 4.0 Tb^{3+} GC.

(F) Schematic of the proposed ML.

observed with the naked eye even in daylight, indicating the high signal-to-noise ratio for stress detection.

The plotted ML intensity versus the applied force of the Ba_2LaF_7: Tb^{3+} GC is assessed in Figure 2B, which suggests a liner dependence of the ML intensity on the imposed force. The identical transitions of $^5D_4 \rightarrow {}^7F_J$ (J = 6, 5, 4, 3) originated from Tb^{3+} ions observed in the ML and PL spectra (Figure S3B) suggest identical emission centers of the involved luminescence procedure. The plotted ML intensity recorded for periodically stress-stimulated Ba_2LaF_7: 4.0 Tb^{3+} GC is depicted in Figure 2C. The intensity of ML exhibits a significant decrease under periodic stress stimulation. The ML intensity is preserved above 95% of the original value after recharging with UV irradiation. The dynamic pressure mapping is illustrated in Figure 2D as the handwritten letters "ML." By extracting and analyzing the grayscale of the captured image, a three-dimensional distribution of the light intensity could be obtained, as shown at the bottom of Figure 2D. The TL curve of Ba_2LaF_7: 4.0 Tb^{3+} GC recorded in Figure 2E presents two respective peaks at 350 and 479 K after Gaussian fitting, suggesting that there are two types of traps in the Ba_2LaF_7: 4.0 Tb^{3+} GC. According to the equation E = T/500 (K) for electron trap depth calculation,[27] where E is the thermo-active energy of trap depth (eV) denoting the energy gap between the electron trap and the conduction band and T is the

temperature for the TL peak maximum, electron traps with a depth of 0.70 and 0.96 eV of Ba_2LaF_7: 4.0 Tb^{3+} GC could be deduced, respectively. Generally, carriers in deep traps ($\geq$0.80 eV) are difficult to release under thermal disturbance at room temperature. As a result, the TL intensity corresponding to the deep trap of Ba_2LaF_7: 4.0 Tb^{3+} GC decreases by 10% after the corresponding sample was deposited at room temperature for 5 days (Figure S6B), which contributes to the insignificant change of ML intensity for the sample re-loaded with 4 N force (Figure S6A). A schematic of the proposed ML is depicted in Figure 2F. After irradiation with a femtosecond laser, the carriers induced by the femtosecond laser are captured by electron traps and hole traps in the matrix,[23,28] respectively. The mechanical energy drives the trapped electrons and holes to be released, and then the released energy is transferred to the luminescence centers of Tb^{3+} ions, which exhibit bright green emission. Other Ln^{3+}-doped Ba_2LaF_7 samples were synthesized, and we measured their TL glow curves for exploration (Figure S7). Compared with that of Ba_2LaF_7:Tb^{3+}, the TL intensity (trap density) of Ba_2LaF_7:Ln^{3+} was much weaker, creating difficulties in exhibiting and observing ML phenomenon.

ML mechanism within the transparent medium

To address the origin of the ML, Ba_2LaF_7: Tb^{3+} NCs and Tb^{3+}-doped glass were prepared for comparison (Figure S8). Figure 3A shows the photoluminescence (PL) spectra of the Ba_2LaF_7: 20% Tb^{3+} NCs, Tb^{3+}-doped glass, and Ba_2LaF_7: 4.0 Tb^{3+} GC, respectively. The shape of the splitting emission peak at 545 nm of the Ba_2LaF_7: 4.0 Tb^{3+} GC is identical to that of Ba_2LaF_7: 20% Tb^{3+} NCs, which is distinct from that of Tb^{3+}-doped glass for the distinct crystal field environments[29,30]. We speculate that the luminescence behavior of Tb^{3+} in the Ba_2LaF_7: 4.0 Tb^{3+} GC mainly originates from the crystal environment of Ba_2LaF_7 rather than that of the amorphous environment of the glass matrix. The PL intensity of the Ba_2LaF_7: 4.0 Tb^{3+} GC is 2.4 and 3.3 times higher than that of Ba_2LaF_7: Tb^{3+} NCs and Tb^{3+}-doped glass samples, respectively (Figure S9), indicating that it fundamentally benefits from the passivation effect of glass on the surface defects of NCs[31,32] and the crystal field environment with low phonon energy provided by the Ba_2LaF_7 host.[33,34] The ML (Figure 3B) and TL (Figure 3C) spectra of the three samples are presented, and the corresponding ML photographs are shown in Figure S10. The Ba_2LaF_7: 20% Tb^{3+} NCs hardly show obvious ML and TL signals because of the absence of an effective defect trap provided by the oxygen vacancy defects of glass, whereas the Tb^{3+}-doped glass presents ML and TL signals because of the effective trap provided by the glass matrix. The Ba_2LaF_7:Tb^{3+} NCs embedded within amorphous glass provide a low phonon lattice environment for Tb^{3+} ions, which contributes to the higher intensities of ML and TL.

The ML and TL intensities of the Ba_2LaF_7: 4.0 Tb^{3+} GC samples with filling and thermal bleaching for 30 cycles are shown in Figure 3D. The ML and TL intensities were preserved above 95% of the initial value after 30 cycles, which confirms that the ML performance of the as-explored GC is reproducible with excellent stability. Figure 3E shows the electron paramagnetic resonance (EPR) spectra of the Ba_2LaF_7: 4.0 Tb^{3+} GC sample before and after irradiation, respectively. An EPR signal is observed at around g = 1.998, ascribed to the oxygen vacancy centers in the glass,[22] after femtosecond laser irradiation (800 nm), and the high-resolution X-ray photoelectron spectroscopy (XPS) O 1s spectra of Ba_2LaF_7: Tb^{3+} GC before and after femtosecond laser irradiation are shown in Figure S11. They confirm that the effective traps in Ba_2LaF_7: 4.0 Tb^{3+} GC originated from the glass matrix rather than Ba_2LaF_7 NCs. The ML spectra of glass@Ba_2LaF_7: 20% Tb^{3+} NCs (a physical

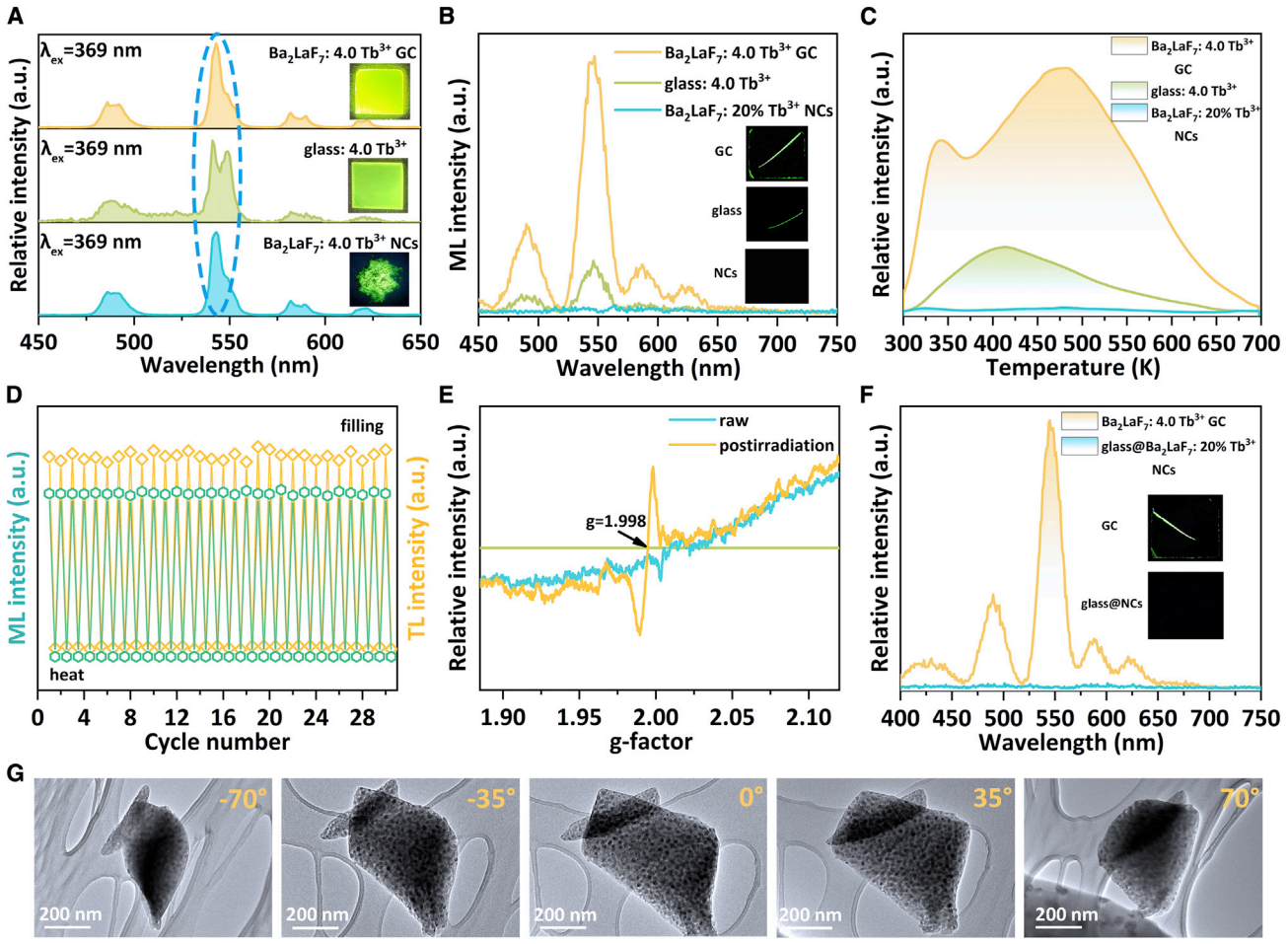

Figure 3. ML behavior originating from the transparent matrix

(A–C) PL (A), ML (B), and TL (C) spectra recorded after irradiation with a femtosecond laser of Ba_2LaF_7: 20% Tb^{3+} NCs, Tb^{3+}-doped glass (glass: 4.0 Tb^{3+}), and Ba_2LaF_7: 4.0 Tb^{3+} GC.

(D) The plotted ML and TL intensity recorded after 30 cycles of laser filling and thermal bleaching.

(E) EPR spectra of the Ba_2LaF_7: 4.0 Tb^{3+} GC before and after femtosecond laser irradiation.

(F) ML spectra of glass@Ba_2LaF_7: 20% Tb^{3+} NCs and Ba_2LaF_7: 4.0 Tb^{3+} GC recorded after 1 min of femtosecond laser irradiation.

(G) TEM images of the Ba_2LaF_7: 4.0 Tb^{3+} GC in three-dimensional rotation (from −70° to 70°) mode (scale bars, 200 nm).

mixture of the aluminosilicate glass powders and Ba_2LaF_7: 20% Tb^{3+} NCs) and Ba_2LaF_7: 4.0 Tb^{3+} GC after femtosecond laser irradiation are shown in Figure 3F. The sample of glass@Ba_2LaF_7: 20% Tb^{3+} NCs hardly shows ML behavior (Figure S13). Hence, we speculate that an efficient energy transfer between the trap centers of the glass to the embedded luminescent centers is indispensable for generation of ML.

The TEM images of Ba_2LaF_7: 4.0 Tb^{3+} GC in three-dimensional rotation (from −70° to 70°) mode are shown in Figure 3G (the corresponding details are illustrated in Figure S12 and Video S5). The strategy of *in situ* growth of Ba_2LaF_7: 4.0 Tb^{3+} NCs from the amorphous structure ensures that the precipitated NCs of Ba_2LaF_7: 4.0 Tb^{3+} are completely embedded within the glass matrix. These encased NCs have direct contact with the glass matrix at the atomic level (Figure 1C), which guarantees efficient energy transfer from the trap centers to the luminescence centers, producing excellent ML.

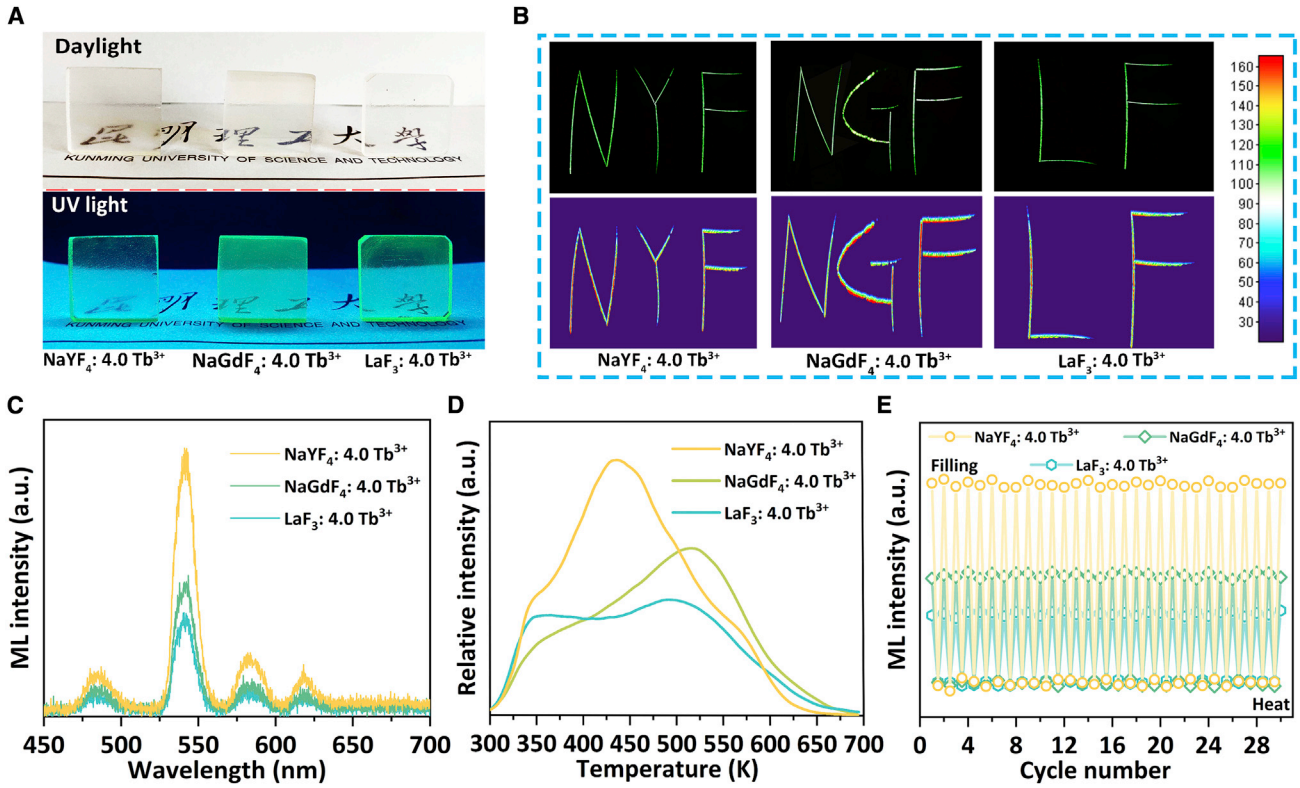

Figure 4. ML originating from $NaYF_4$: 4.0 Tb^{3+}, $NaGdF_4$: 4.0 Tb^{3+}, and LaF_3: 4.0 Tb^{3+} GCs

(A) Photographs recorded under daylight and under 365 nm UV light irradiation.

(B) ML behavior and recorded distribution of the loaded force.

(C) ML spectra.

(D) TL curves.

(E) The plotted ML intensity for 30 cycles of filling and thermal bleaching of the three samples.

ML properties of a series of fluoride GCs

The ML from the transparent GCs could be speculated for the following reasons (Figure S14). First, there are abundant oxygen-deficient centers formed among the amorphous matrix, which would act as effective trap centers.[22–24] Second, a stable crystal field environment provided by the precipitated NCs ensures excellent luminescence performance of the corresponding emission centers. Finally, effective energy transfer between the traps and the luminescence centers is facilitated by atom-atom contact of the encased NCs with the aligned atoms and amorphous structure. Hence, we successfully precipitated $NaYF_4$: 4.0 Tb^{3+}, $NaGdF_4$: 4.0 Tb^{3+}, and LaF_3: 4.0 Tb^{3+} within aluminosilicate glass (Figure S15), and the corresponding photographs of these GC samples under daylight and 365-nm irradiation are shown in Figure 4A. The as-explored fluoride GCs with high transparency exhibit intrinsic green luminescence of Tb^{3+} under UV (369 nm) irradiation (Figure S16). These GC samples show excellent ML behavior (Figures 4B–4E), consistent with the performance of the Ba_2LaF_7: 4.0 Tb^{3+} GC. This demonstrates that the *in situ* growth strategy proposed in this work to design transparent mechanoluminescent GCs is feasible.

Real-time self-driven stress detection

As a proof-of concept experiment, a bare fiber with superb flexibility was obtained by manually drawing from the glass melt, as depicted in Figure 5A, which has a diameter of ≈320 μm and a length of ≈2 m. The optical waveguide properties of

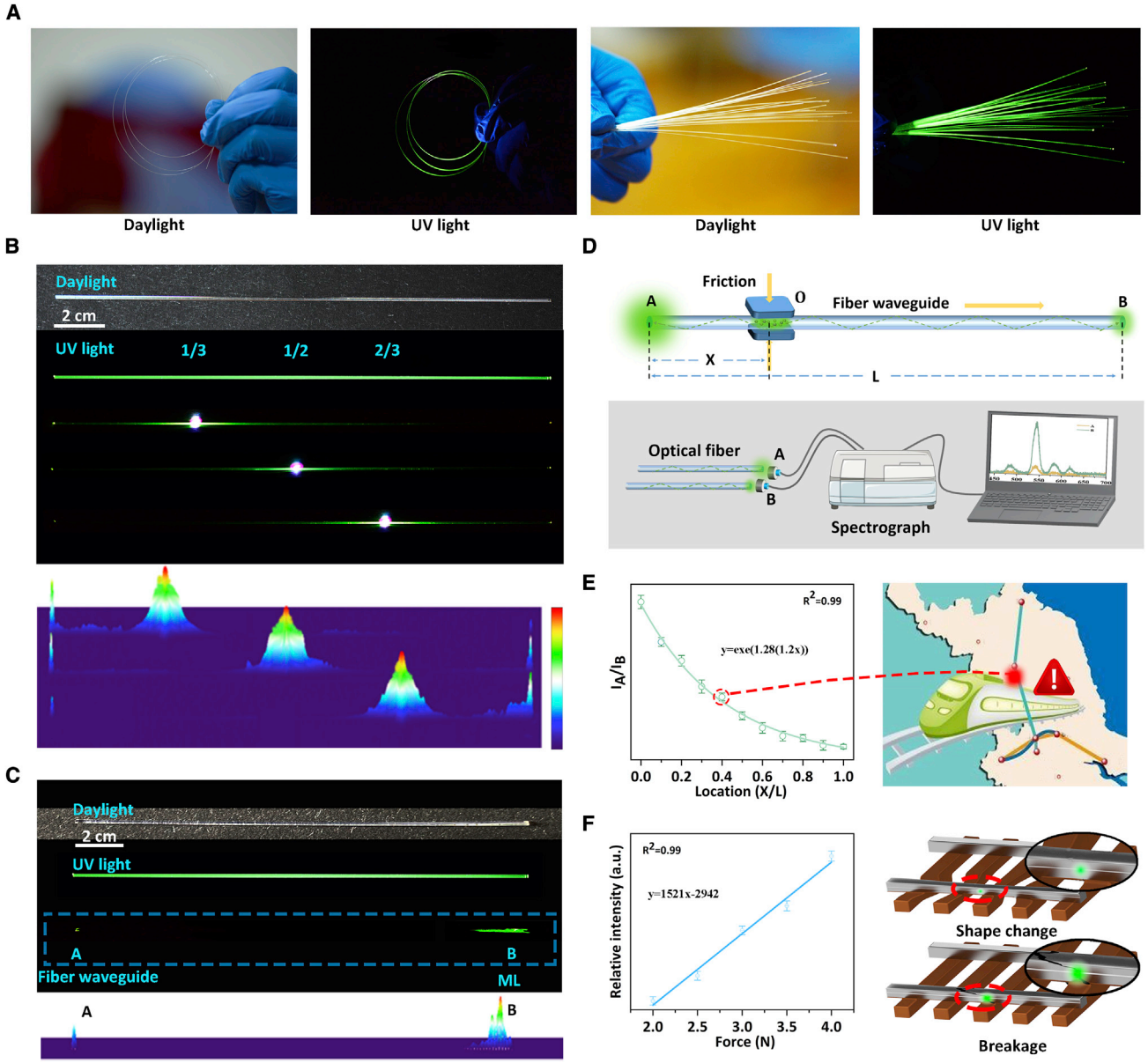

Figure 5. Real-time stress detection based on the optical waveguide characteristics of the as-explored GC fiber

(A) Photographs of the corresponding GC fiber under daylight.

(B) Photographs of the GC fiber under UV light excitation, with the recorded optical waveguide behavior at different locations.

(C) Photographs of the GC fiber under friction stimulation.

(D) Schematic of the as-developed stress sensor system.

(E) The plotted ratio of the fluorescence intensity at the two ends of A and B, dependent on the location of loaded stress.

(F) ML intensity versus the loaded force.

the as-obtained optical fiber are evaluated as shown in Figure 5B. When the pulse laser (365 nm) is employed at different locations, the corresponding PL intensity is observed accordingly. The optical waveguide behavior is performed for observation of the luminescence at both ends of the fiber,[35,36] which confirms the uniformity of the as-explored fiber. Figure 5C shows that the bright green luminescence could be captured at point A when an ML signal is produced at point B of the as-obtained fiber. The corresponding light intensity is illustrated at the bottom of Figure 5C. The

excellent optical waveguide phenomenon of the as-explored ML transparent medium is demonstrated (Figure S18) because of the high transparency (Figure S2A) and inhibited self-absorption effect (Figure S17).

The characteristics of optical waveguides to realize friction detection via transmission of the corresponding optical signals is depicted in Figure 5D. Given a stress-induced ML at point O, green luminescence can be observed at points A and B of the fiber. According to the plotted fluorescence intensity ratio of the A and B locations of loaded stress, the accurate location of the stress can be determined (Figure 5E). The stress strength of the detected location can be determined by the fluorescence intensity of the two locations, and the derivation process is illustrated in the supplemental information. Figure 5F shows the plotted ML intensity versus the loaded force, the linear relationship of which suggests that the loaded force of the fiber could be inferred from the captured optical signals. The high physical and chemical stability of the self-driven optical fiber sensor with the real-time response and high reliability is displayed in Figure S19 for operation in harsh environments.

Bright green ML from a highly transparent GC is realized in this work. It demonstrates unambiguously that *in situ* precipitation of Ba_2LaF_7:Tb^{3+} encased in a transparent medium not only ensures energy transfer between the traps and the luminescence centers but also reduces the light scattering loss because of the growth restriction of the corresponding NCs. The fascinating optical waveguide effect of the explored GC enables the possibility of remote and real-time capture of stress signals. We believe that this optical transparent sensor shows promise for reliable detection, propagation, and recording of force information, which could open a new window for stress detection.

EXPERIMENTAL PROCEDURES

Resource availability

Lead contact

Further information and requests for resources should be directed to and will be fulfilled by the lead contact, Xuhai Xu. (xuxuh07@126.com).

Materials availability

This study did not generate new unique materials.

Data and code availability

Data reported in this paper are available from the lead contact upon reasonable request. No new code was developed in this study.

Material fabrication

Ba_2LaF_7: Tb^{3+} GC samples were synthesized by a melting-quenching procedure. The glass matrix was designed with molar compositions of $45SiO_2$-$15Al_2O_3$-$12Na_2CO_3$-$21BaF_2$-(7-x)LaF_3-xTbF_3, which was named Ba_2LaF_7: xTb^{3+}. The raw materials of SiO_2 (99.99%), Al_2O_3 (99.99%), Na_2CO_3 (99.9%), BaF_2 (99.99%), LaF_3 (99.9%), and high-purity TbF_3 (99.99%) were well mixed and ground into powders with an agate mortar and pestle. Then the well-ground stoichiometric compounds were put into an alumina crucible and melted at 1,450°C for 45 min in an air atmosphere. After that, the melt was poured onto a 350°C preheated stainless steel plate and then pressed by another brass plate to form a precursor glass. The precursor glasses were annealed in a muffle furnace at 480°C for 8 h to release the thermal stress. Subsequently, these precursor glasses were heat-treated for 2 h at 640°C to form transparent Ba_2LaF_7 GCs. The Tb^{3+}-doped Ba_2LaF_7 GC products were

polished or ground into powders for further characterization. The corresponding glass optical fibers were obtained directly by manually drawing from molten glass, with a diameter of ≈320 μm and a length of ≈2 m. In a comparison, Ba_2LaF_7: 20%Tb^{3+} NCs were synthesized using a hydrothermal method (Figure S20). An aqueous solution of NaOH (6 mmol) was added into 20 mL oleic acid containing 10 mL ethanol under vigorous stirring to form a transparent homogeneous solution, followed by addition of an aqueous solution of 0.4 mmol $La(NO_3)_3$ and 0.1 mmol $Tb(NO_3)_3$. After 10 min, 0.5 mmol of $BaCl_2$ (0.5 M) and 2 mmol of NH_4F (4 M) aqueous solutions were added in turn to the above mixed solution. The resulting mixture was then transferred into a 50-mL Teflon-lined autoclave and heated at 180°C for 12 h after stirring for 30 min. Then the corresponding products were collected by centrifugation and washed several times with ethanol and cyclohexane at room temperature. The final products were dispersed by cyclohexane for characterization.

Material characterization

The phase samples were identified via XRD measurement (D8ADVANCE/Germany Bruker X-ray diffractometer), with Cu-Kα radiation (λ = 0.15405 nm) in the 2θ range from 10°–80°. The microstructure of the GCs was analyzed by TEM and HR-TEM using a JEM-F200 operating at 200 kV. Sample morphology and the energy-dispersive spectrum (EDS) were measured using a scanning electron microscope (JEOL JIB-4700F). The PL and PL excitation (PLE) spectra were recorded with a Hitachi F-7000 fluorescence spectrophotometer with a 150-W Xe lamp as the excitation source. The transmittance spectra and absorption spectra were recorded in the wavelength range from 200–800 nm by a Hitachi U-4100 type spectrophotometer. The decay curves of Ba_2LaF_7: Tb^{3+} GC were recorded by a time-resolved fluorescence spectrophotometer (FLS920, Edinburgh Instrument, Edinburgh, UK). The TL curves were measured with an FJ-427A TL meter (Beijing Nuclear Instrument Factory, Beijing, China). The EPR spectra of the samples were measured by a Bruker X-band A300-6/1 paramagnetic resonance spectrometer at a frequency of 9.2 GHz and room temperature. XPS analysis was carried out using a Thermo Fisher Scientific K-Alpha and an Al-Kα X-ray source (hυ = 1486.6 eV) with a 400-μm spot size and 30-eV pass energy. A regeneratively amplified 800 nm Ti: sapphire laser with 120-fs, 200-kHz, mode-locked pulses was employed in this work. The laser beam, with an average power of 2.3 W, was focused by a 100-mm focal length lens on the glass samples with the help of an XYZ stage. ML signals were collected *in situ* from a rotary friction testing machine (MS-T3001) to a fluorescence spectrophotometer (Omni-λ300i, Zolix Instruments) equipped with a camera (iVac-316, Edmund Optics) as depicted in Figure S21. All optical photographs were taken by a Nikon D7100 digital camera with AF-S Micro-Nikkor 105-mm f/2.8G IF-ED during the daytime indoors (marked "daylight") or under dark conditions.

In situ solid-cell TEM imaging

The measurement of *in situ* TEM, HR-TEM was performed by a JEM-F200 field emission transmission electron microscope with 200-kV electron energy, and the recorded images were captured by a Gatan SC1000 ORIUS charge-coupled device (CCD) camera with an exposure time of 0.5 s/frame. The electron beam with a current density of 60 pA, where an electron flux of 2.9 × 102 e-Å-2 s-1 at × 50,000 magnification, was employed. Electron flux was kept constant for each experiment, and the E-beam was modulated by varying the irradiation size. *In situ* TEM images of the solid cells were recorded at room temperature with the changed E-beam intensity to monitor the growth and degradation of the corresponding samples.

SUPPLEMENTAL INFORMATION

Supplemental information can be found online at https://doi.org/10.1016/j.xcrp.2022.101093.

ACKNOWLEDGMENTS

This work was financially supported by the National Nature Science Foundation of China (NSFC) (61965012), Yunnan Provincial Natural Science Foundation (202001AS070008 and 202101AT070126), Sichuan Provincial Natural Science Foundation (2022JDJQ0030), Yunnan Ten Thousand Talents Plan Young & Elite Talents Project (YNWR-QNBJ-2018-295), Excellent Youth Project of Yunnan Province Applied Basic Research Project (2019FI001), and Yunnan Major Scientific and Technological Projects (202202AG050004).

AUTHOR CONTRIBUTIONS

X.Y., X.X., and Z.W. conceived the idea and supervised the project. H.T. and L.Z. designed the experiments, fabricated the Ba_2LaF_7: GC, and carried out characterization of Ba_2LaF_7: GC. H.T., L.Z., Q.P., T.W., and Z.L. analyzed the data of Ba_2LaF_7: GC characterization. H.T. wrote the first draft of the manuscript with input from Y.B., M.D., F.Z., J.Q., X.Y., Q.W., and X.X. All authors reviewed, commented on, and revised the manuscript.

DECLARATION OF INTERESTS

The authors declare no competing interests.

Received: July 22, 2022
Revised: August 7, 2022
Accepted: September 14, 2022
Published: October 19, 2022

REFERENCES

1. Westerveld, W.J., Mahmud-Ul-Hasan, M., Shnaiderman, R., Ntziachristos, V., Rottenberg, X., Severi, S., and Rochus, V. (2021). Sensitive, small, broadband and scalable optomechanical ultrasound sensor in silicon photonics. Nat. Photonics *15*, 341–345. https://doi.org/10.1038/s41566-021-00776-0.

2. Lee, S., Reuveny, A., Reeder, J., Lee, S., Jin, H., Liu, Q., Yokota, T., Sekitani, T., Isoyama, T., Abe, Y., et al. (2016). A transparent bending-insensitive pressure sensor. Nat. Nanotechnol. *11*, 472–478. https://doi.org/10.1038/nnano.2015.324.

3. Meng, K., Xiao, X., Wei, W., Chen, G., Nashalian, A., Shen, S., Xiao, X., and Chen, J. (2022). Wearable pressure sensors for pulse wave monitoring. Adv. Mater. *34*, e2109357. https://doi.org/10.1002/adma.202109357.

4. Wei, H.-Z., Xu, D.-S., and Meng, Q.-S. (2018). A newly designed fiber-optic based earth pressure transducer with adjustable measurement range. Sensors *18*, 932. https://doi.org/10.3390/s18040932.

5. Xie, M., Zhang, Y., Krašny, M.J., Bowen, C., Khanbareh, H., and Gathercole, N. (2018). Flexible and active self-powered pressure, shear sensors based on freeze casting ceramic–polymer composites. Energy Environ. Sci. *11*, 2919–2927. https://doi.org/10.1039/c8ee01551a.

6. Han, X., Du, W., Chen, M., Wang, X., Zhang, X., Li, X., Li, J., Peng, Z., Pan, C., and Wang, Z.L. (2017). Visualization recording and storage of pressure distribution through a smart matrix based on the piezotronic effect. Adv. Mater. *29*, 1701253. https://doi.org/10.1002/adma.201701253.

7. Vorathin, E., Hafizi, Z.M., Ismail, N., and Loman, M. (2020). Review of high sensitivity fibre-optic pressure sensors for low pressure sensing. Opt Laser. Technol. *121*, 105841. https://doi.org/10.1016/j.optlastec.2019.105841.

8. Lindsey, N.J., Dawe, T.C., and Ajo-Franklin, J.B. (2019). Illuminating seafloor faults and ocean dynamics with dark fiber distributed acoustic sensing. Science *366*, 1103–1107. https://doi.org/10.1126/science.aay5881.

9. Bai, H., Li, S., Barreiros, J., Tu, Y., Pollock, C.R., and Shepherd, R.F. (2020a). Stretchable distributed fiber-optic sensors. Science *370*, 848–852. https://doi.org/10.1126/science.aba5504.

10. Zhuang, Y., and Xie, R.J. (2021). Mechanoluminescence rebrightening the prospects of stress sensing: a Review. Adv. Mater. *33*, 2005925. https://doi.org/10.1002/adma.202005925.

11. Song, F., Xie, A.J., and Seo, S.-W. (2014). Elastomeric polymer resonant waveguide grating based pressure sensor. J. Opt. *16*, 065702. https://doi.org/10.1088/2040-8978/16/6/065702.

12. Zhuang, Y., Tu, D., Chen, C., Wang, L., Zhang, H., Xue, H., Yuan, C., Chen, G., Pan, C., Dai, L., and Xie, R.J. (2020). Force-induced charge carrier storage: a new route for stress recording. Light Sci. Appl. *9*, 182. https://doi.org/10.1038/s41377-020-00422-4.

13. Chen, C., Zhuang, Y., Li, X., Lin, F., Peng, D., Tu, D., Xie, A., and Xie, R. (2021). Achieving remote stress and temperature dual-modal imaging by double-lanthanide-activated mechanoluminescent materials. Adv. Funct. Mater. *31*, 2101567. https://doi.org/10.1002/adfm.202101567.

14. Wu, C., Zeng, S., Wang, Z., Wang, F., Zhou, H., Zhang, J., Ci, Z., and Sun, L. (2018). Efficient mechanoluminescent elastomers for dual-responsive anticounterfeiting device and stretching/strain sensor with multimode sensibility. Adv. Funct. Mater. *28*, 1803168. https://doi.org/10.1002/adfm.201803168.

15. Tian, B., Wang, Z., Smith, A.T., Bai, Y., Li, J., Zhang, N., Xue, Z., and Sun, L. (2021). Stress-induced color manipulation of mechanoluminescent elastomer for visualized mechanics sensing. Nano Energy *83*, 105860. https://doi.org/10.1016/j.nanoen.2021.105860.

16. Shohag, M.A.S., Eze, V.O., Braga Carani, L., and Okoli, O.I. (2020). Fully integrated mechanoluminescent devices with nanometer-thick perovskite film as self-powered flexible sensor for dynamic pressure sensing. ACS Appl. Nano Mater. *3*, 6749–6756. https://doi.org/10.1021/acsanm.0c01168.

17. Wang, X., Que, M., Chen, M., Han, X., Li, X., Pan, C., and Wang, Z.L. (2017). Sensors: full dynamic-range pressure sensor matrix based on optical and electrical dual-mode sensing. Adv. Mater. *29*, 1605817. https://doi.org/10.1002/adma.201605817.

18. Du, Y., Jiang, Y., Sun, T., Zhao, J., Huang, B., Peng, D., and Wang, F. (2019). Mechanoluminescence: mechanically excited multicolor luminescence in lanthanide ions. Adv. Mater. *31*, 1970051. https://doi.org/10.1002/adma.201970051.

19. Xiong, P., Huang, B., Peng, D., Viana, B., Peng, M., and Ma, Z. (2021). Self-recoverable mechanically induced instant luminescence from Cr^{3+}-doped $LiGa_5O_8$. Adv. Funct. Mater. *31*, 2010685. https://doi.org/10.1002/adfm.202010685.

20. Tu, D., Xu, C.-N., Yoshida, A., Fujihala, M., Hirotsu, J., and Zheng, X.-G. (2017). $LiNbO_3$:Pr^{3+}: a multipiezo material with simultaneous piezoelectricity and sensitive piezoluminescence. Adv. Mater. *29*, 1606914. https://doi.org/10.1002/adma.201606914.

21. Zhang, J.-C., Wang, X., Marriott, G., and Xu, C.-N. (2019). Trap-controlled mechanoluminescent materials. Prog. Mater. Sci. *103*, 678–742. https://doi.org/10.1016/j.pmatsci.2019.02.001.

22. Ueda, J., Hashimoto, A., and Tanabe, S. (2019). Orange persistent luminescence and photodarkening related to paramagnetic defects of nondoped CaO-Ga_2O_3-GeO_2 Glass. J. Phys. Chem. C *123*, 29946–29953. https://doi.org/10.1021/acs.jpcc.9b07638.

23. Girard, S., Alessi, A., Richard, N., Martin-Samos, L., De Michele, V., Giacomazzi, L., Agnello, S., Francesca, D.D., Morana, A., Winkler, B., et al. (2019). Overview of radiation induced point defects in silica-based optical fibers. Rev. Phys. *4*, 100032. https://doi.org/10.1016/j.revip.2019.100032.

24. Luo, H., Cao, J., Li, X., Wang, X., and Peng, M. (2018). Topological tailoring of structure and defects to enhance red to near-infrared afterglow from Mn^{2+}-doped germanate photonic glasses. J. Mater. Chem. C *6*, 11525–11535. https://doi.org/10.1039/c8tc03477j.

25. Cao, L.-Y., Si, S.-C., Yu, J.-B., Ma, C.-G., Qiu, J.-B., and Wang, J. (2021). A precisely space-separated strategy of donor-acceptor for intense red emitting composite borosilicate glass co-doped with $CsPbCl_3$ quantum dots and Mn^{2+} ions. Chem. Eng. J. *417*, 129177. https://doi.org/10.1016/j.cej.2021.129177.

26. Zhang, H., Yang, Z., Zhou, M., Zhao, L., Jiang, T., Yang, H., Yu, X., Qiu, J., Yang, Y.M., Xu, X., and Xu, X. (2021). Reproducible x-ray imaging with a perovskite nanocrystal scintillator embedded in a transparent amorphous network structure. Adv. Mater. *33*, 2102529. https://doi.org/10.1002/adma.202102529.

27. Huang, K., Dou, X., Zhang, Y., Gao, X., Lin, J., Qu, J., Li, Y., Huang, P., and Han, G. (2021). Enhancing light and x-ray charging in persistent luminescence nanocrystals for orthogonal afterglow anti-counterfeiting. Adv. Funct. Mater. *31*, 2009920. https://doi.org/10.1002/adfm.202009920.

28. Qiu, J., Miura, K., Inouye, H., Kondo, Y., Mitsuyu, T., and Hirao, K. (1998). Femtosecond laser-induced three-dimensional bright and long-lasting phosphorescence inside calcium aluminosilicate glasses doped with rare earth ions. Appl. Phys. Lett. *73*, 1763–1765. https://doi.org/10.1063/1.122274.

29. Liu, Y., Tu, D., Zhu, H., and Chen, X. (2013). Lanthanide-doped luminescent nanoprobes: controlled synthesis, optical spectroscopy, and bioapplications. Chem. Soc. Rev. *42*, 6924–6958. https://doi.org/10.1039/c3cs60060b.

30. Assadi, A.A., Herrmann, A., Tewelde, M., Damak, K., Maalej, R., and Rüssel, C. (2018). Tb^{3+} as a probe for the molecular structure of mixed barium magnesium alumino silicate glasses. J. Lumin. *199*, 384–390. https://doi.org/10.1016/j.jlumin.2018.03.012.

31. Wang, T., Liu, B., Lin, Y., Yang, Q., Gao, W., Li, M.J., Qiu, J., Yu, X., Xu, X., and Yu, S.F. (2020). Ultraviolet C lasing at 263 nm from Ba_2LaF_7:Yb^{3+}, Tm^{3+} upconversion nanocrystal microcavities. Opt. Lett. *45*, 5986–5989. https://doi.org/10.1364/ol.401768.

32. Zhang, H., Yang, Z., Zhao, L., Cao, J., Yu, X., Yang, Y.M., Yu, S., Qiu, J., Xu, X., and Xu, X. (2020). Long persistent luminescence from all-inorganic perovskite nanocrystals. Adv. Opt. Mater. *8*, 2000585. https://doi.org/10.1002/adom.202000585.

33. Xu, X., Zhang, W., Yang, D., Lu, W., Qiu, J., and Yu, S.F. (2016). Phonon-assisted population inversion in lanthanide-doped upconversion Ba_2LaF_7 nanocrystals in glass-ceramics. Adv. Mater. *28*, 8045–8050. https://doi.org/10.1002/adma.201601405.

34. Xu, C.f., Ma, M., Yang, L.w., Zeng, S.j., and Yang, Q.b. (2012). Lanthanide doping-facilitated growth of ultrasmall monodisperse Ba_2LaF_7 nanocrystals with excellent photoluminescence. J. Colloid Interface Sci. *368*, 49–55. https://doi.org/10.1016/j.jcis.2011.10.072.

35. Liu, B., Di, Q., Liu, W., Wang, C., Wang, Y., and Zhang, H. (2019a). Red-emissive organic crystals of a single-benzene molecule: elastically bendable and flexible optical waveguide. J. Phys. Chem. Lett. *10*, 1437–1442. https://doi.org/10.1021/acs.jpclett.9b00196.

36. Ding, Z., Shang, H., Geng, Y., Zhang, S.-T., Huo, Z., Yang, Z., Li, B., Xu, W., and Jiang, S. (2021). Tuning organic microcrystal morphologies through crystal engineering strategies toward anisotropic optical waveguide. J. Phys. Chem. Lett. *12*, 4585–4592. https://doi.org/10.1021/acs.jpclett.1c00769.